Shear thickening and history-dependent rheology of monodisperse suspensions with finite inertia via an immersed boundary lattice Boltzmann method

Srinivasan, Sudharsan; Van den Akker, Harry E.A.; Shardt, Orest

DOI
10.1016/j.ijmultiphaseflow.2019.103205

Publication date
2020

Document Version
Accepted author manuscript

Published in
International Journal of Multiphase Flow

Citation (APA)
Srinivasan, S., Van den Akker, H. E. A., & Shardt, O. (2020). Shear thickening and history-dependent rheology of monodisperse suspensions with finite inertia via an immersed boundary lattice Boltzmann method. *International Journal of Multiphase Flow*, *125*, Article 103205. https://doi.org/10.1016/j.ijmultiphaseflow.2019.103205

Shear thickening and history-dependent rheology of monodisperse suspensions with finite inertia via an immersed boundary lattice Boltzmann method

Sudharsan Srinivasan[a,b,*], Harry E.A. Van den Akker[a,b,c], Orest Shardt[a,b,*]

[a] *Synthesis and Solid State Pharmaceutical Centre (SSPC), University of Limerick, V94T9PX, Limerick, Ireland*
[b] *Bernal Institute, University of Limerick, V94T9PX, Limerick, Ireland*
[c] *Transport Phenomena Lab, Department of Chemical Engineering, Delft University of Technology, Van der Maasweg 9, 2629 HZ Delft, The Netherlands*

Abstract

Three-dimensional direct numerical simulations of dense suspensions of monodisperse spherical particles in simple shear flow have been performed at particle Reynolds numbers between 0.1 and 0.6. The particles translate and rotate under the influence of the applied shear. The lattice Boltzmann method was used to solve the flow of the interstitial Newtonian liquid, and an immersed boundary method was used to enforce the no-slip boundary condition at the surface of each particle. Short range spring forces were applied between colliding particles over sub-grid scale distances to prevent overlap. We computed the relative apparent viscosity for solids volume fractions up to 38% for several shear rates and particle concentrations and discuss the effects of these variables on particle rotation and cluster formations. The apparent viscosities increase with increasing particle Reynolds number (shear thickening) and solids fraction. As long as the particle Reynolds number is low (0.1), the computed viscosities are in good agreement with experimental measurements, as well

*Corresponding authors.
E-mail address: Sudharsan.Srinivasan@ul.ie, Orest.Shardt@ul.ie

as theoretical and empirical equations. For higher Reynolds numbers, we find much higher viscosities, which we relate to slower particle rotation and clustering. Simulations with a sudden change in shear rate also reveal a history (or hysteresis) effect due to the formation of clusters. We quantify the changes in particle rotation and clustering as a function of Reynolds number and volume fraction.
Keywords: rheology; suspensions; immersed boundary method; lattice Boltzmann method; shear flow

1. Introduction

Suspensions are heterogeneous mixtures of solid particles suspended in a bulk fluid medium (Rietema, 1982; Barnes et al., 1989). Flows of such suspensions are encountered in our daily lives and many industrial applications in chemical, biochemical, aerospace and environmental engineering. Many researchers have studied the flow behaviour of suspensions, both experimentally and by means of models and computational simulations. Examples of the latter include direct analysis of particle motion in suspensions (Aidun et al., 1998), particle dynamics in dense crystal slurries (Ten Cate et al., 2004), sedimentation of blood cells (Shardt and Derksen, 2012), mixing of suspended particles in stirred tanks (Derksen, 2003, 2018), and transport of slurries with fine particles (Yoshida et al., 2013). When dense suspensions flow through pipelines, they exhibit various forms of non-Newtonian behaviour that depend on the interactions of particles with each other and with the surrounding liquid. An understanding of the rheological behaviour of these suspensions is therefore necessary for many practical industrial applications.

The rheology of suspensions may be classified into different categories: shear

thinning, shear thickening, yield stress (Bingham), yield stress shear thinning (Herschel Bulkley), and time dependent (thixotropic) (Barnes et al., 1989). The apparent viscosity of a fluid may depend upon various factors such as shear rate, particle concentration, size distribution and shape, interparticle forces, and time of shearing. The dynamic interactions of particles based on these factors determine the suspension microstructure, from which the macroscopic rheological properties emerge (Brady and Bossis, 1985). An important challenge is to determine how these complex physicochemical interactions affect rheology.

Predicting the rheological behaviour of suspensions has been a long-standing research problem (Einstein, 1906; Batchelor and Green, 1972; Mueller et al., 2009; Yoshida et al., 2013). The theoretical estimation of the relative apparent viscosity (the ratio of the effective viscosity of a suspension and the viscosity of the suspending fluid) for a dilute suspension of rigid spheres in simple shear flow in the Stokes regime originated from the work of Einstein (1906). Further extensions to Einstein's formula by considering the effects of particle interactions have also been developed via experiments and theory (Vand, 1948; Krieger and Dougherty, 1959; Peterson and Fixman, 1963; Frankel and Acrivos, 1967; Batchelor and Green, 1972; Brady and Bossis, 1985). Suspension viscosity is usually measured in rheometers of different working principles, such as flow through an orifice or a capillary, the falling rate of a piston or a ball, the response to an imposed vibration, or a Couette flow. The value of the suspension viscosity may depend on the way it is measured. A recent review of the rheology of dense granular suspensions by Guazzelli and Pouliquen (2018) compared the viscosities due to several experimental and theoretical correlations.

The review also considered how suspensions respond to changes in the flow, such as a reversal in the shear direction (see also Gadala and Acrivos (1980)) .

In this paper, we focus on numerical simulations of translating and rotating solid spherical particles in simple shear flow. An advantage of running computational simulations over conducting experiments with the view of determining suspension viscosities is that simulations allow far better control of the various parameters that contribute to the complex interactions between particles and liquid. Not only do these parameters comprise physical properties such as particle and fluid density, particle size and concentration and liquid viscosity, but also flow parameters such as the imposed flow rate and local shear rate. In simulations, we can vary the relevant parameters independently, with the view of distinguishing their separate effects on suspension viscosity. In addition, simulations allow us to look 'inside' dense suspensions to learn more about, for example, clustering behaviour as a function of particle concentration, which is not possible in experiments. As an example of looking inside a suspension, Derksen et al. (2015) used an immersed boundary method to simulate the dissolution of spherical particles in laminar shear flow.

We perform computational simulations of shear-induced suspension behaviour using the lattice Boltzmann method (LBM) and determine the relative apparent viscosity of the suspensions η_r from the shear stress on the walls,

$$\eta_r = \frac{\langle \tau \rangle}{\mu \dot{\gamma}} \tag{1}$$

where $\langle \tau \rangle$ is the average shear stress evaluated along a sliding wall, μ is the dynamic viscosity of the interstitial liquid, and $\dot{\gamma}$ is the shear rate. We discuss the observed rheology, emphasising the effects of shear rate, particle concentration, particle rota-

tion, clustering, and sudden changes in the shear rate.

This paper is organised as follows: We first define the flow system and the relevant dimensionless parameters. Then we discuss the fluid flow solver, the numerical method used to enforce the no-slip boundary condition on the surface of each particle, and the integration scheme for the translational and rotational motion of the particles. We then describe a forcing scheme for handling particle collisions. Next, we discuss several validations of the numerical method before comparing the simulation viscosities of dense suspensions with theoretical equations and empirical correlations. We study the effects of shear rate, particle concentration, and changes in the shear rate on the apparent viscosity of the suspension. We discuss the role particle rotation and clustering on the observed viscosity. We discuss the relationship between the apparent viscosities, the rotation rates of individual particles, and the extent of clustering within the sheared suspension. Finally, we summarise our findings in the conclusions.

2. Numerical methods

2.1. Flow system

The purpose of our research is to develop expressions for the dependence of the apparent viscosity of a suspension on the shear rate (or particle Reynolds number) and solids volume fraction with the view of predicting the transport behaviour of dense slurries through industrial pipelines. The size of the particles in these slurries is 150 to 300 μm, and the solids volume fraction ϕ_v amounts to 35%. Our approach towards this goal is to run, for a small parcel of a slurry, numerical simulations of many monodisperse neutrally buoyant rigid spheres placed initially randomly in a simple shear flow, as shown in Fig. 1. The liquid phase is Newtonian with kinematic

viscosity ν. The simulation domain is periodic in x and y, which means that the liquid and solids leaving one end of the domain re-enter from the opposite end. The top and bottom (z-direction) $x-y$ planes are sheared in opposite directions with an overall shear rate $\dot{\gamma} = 2U_w/H$, where U_w is the wall speed and H is the distance between the walls. The liquid and solids are at rest initially and the flow is induced only by the shearing motion of the walls.

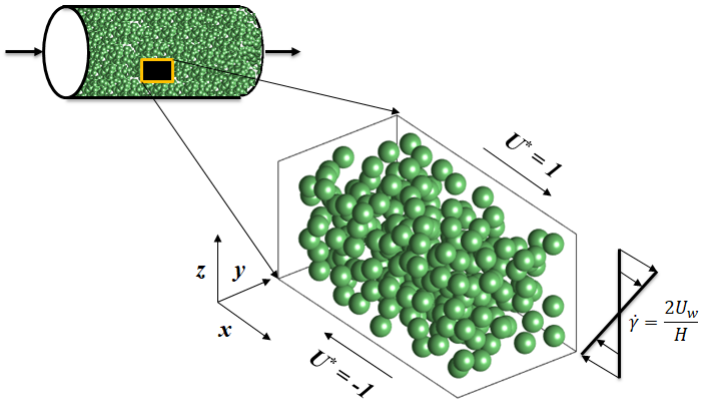

Figure 1: Schematic of the simulated monodisperse suspension. $U^* = U_x/U_w$ is the dimensionless fluid velocity with U_x being the x component of the fluid velocity.

In order to match the simulations with physical systems, the following dimensionless parameters were considered: the particle Reynolds number $Re_p = \dot{\gamma}R^2/\nu$, (where R is the particle radius), and the confinement ratio $\delta = 2R/H$ (where H is the domain height). We study the rheological behaviour of suspensions with $2\% \leq \phi_v \leq 38\%$. In order to match the conditions relevant to the pipeline application, we consider the range of particle Reynolds numbers $0.11 \leq Re_p \leq 0.55$.

2.2. Flow solver

We use LBM to solve the flow of the interstitial Newtonian liquid (Chen and Doolen, 1998; Krüger et al., 2017). LBM is an explicit time marching finite difference scheme for the continuous Boltzmann equation. This method uses a regular

cubic lattice, where the fluid is described by fictitious particles (populations f_i) that move with discrete velocities $\mathbf{c}_i$. Forces may be applied to these particles, and momentum transport occurs when the particles stream from each lattice node to the neighbouring lattice nodes and collide with each other according to the BGK collision operator (Bhatnagar et al., 1954). The simulations are three-dimensional and we use a *D3Q19* (three-dimensional with 19 velocities) LB model. The populations evolve according to the discrete Boltzmann equation

$$f_i(\mathbf{x} + \mathbf{c}_i\Delta t, t + \Delta t) = f_i(\mathbf{x}, t) - \frac{\Delta t}{\tau}(f_i(\mathbf{x}, t) - f_i^{eq}(\mathbf{x}, t)) \tag{2}$$

where the subscript i counts over the number of discrete velocities. τ is the relaxation time, t is the simulation time, $\Delta t = 1$ is the time step. The equilibrium distribution function is

$$f_i^{eq}(\mathbf{x}, t) = w_i\rho\left(1 + 3(\mathbf{u}\cdot\mathbf{c}_i) + \frac{9}{2}(\mathbf{u}\cdot\mathbf{c}_i)^2 - \frac{3}{2}(\mathbf{u}\cdot\mathbf{u})\right), \tag{3}$$

where the values of the weights are: $w_0 = \frac{1}{3}$, $w_{1-6} = \frac{1}{18}$, and $w_{7-18} = \frac{1}{36}$. At each lattice node, the density of the fluid $\rho(\mathbf{x}, t)$ and the velocity $\mathbf{u}(\mathbf{x}, t)$ are computed from the populations according to:

$$\rho(\mathbf{x}, t) = \sum_i f_i(\mathbf{x}, t) \tag{4}$$

and

$$\mathbf{u}(\mathbf{x}, t) = \frac{1}{\rho(\mathbf{x}, t)}\sum_i f_i(\mathbf{x}, t)\mathbf{c}_i + \frac{\mathbf{F}(\mathbf{x}, t)\Delta t}{2\rho(\mathbf{x}, t)} \tag{5}$$

where $\mathbf{F}(\mathbf{x}, t)$ is the Eulerian force density per unit volume. This body force is incorporated in the LBM simulation using the Shan and Chen (1993) forcing scheme, which modifies the velocity used to calculate the equilibrium distribution. The fluid

kinematic viscosity ν is related to the relaxation time by

$$\nu = \frac{2\tau - 1}{6}. \tag{6}$$

To simulate incompressible flow with LBM, we require that the Mach number $Ma \ll 1$. The shear speed in the simulations does not exceed 0.025 lu/ts (where lu is lattice spacing and ts is lattice time), and it is therefore well below the speed of sound $c_s = 1/\sqrt{3}$ in LBM.

2.3. Boundary conditions

To enforce the no-slip boundary condition for the moving walls, we used a bounce back scheme with momentum correction (Ladd, 1994). The no-slip boundary condition on the surface of each finite-sized particle is implemented by means of an immersed boundary method (IBM). Several variants of IBM have been developed over the past two decades: Derksen and Van den Akker (1999); Rohde et al. (2002); Ten Cate et al. (2004); Feng and Michaelides (2004); Tschisgale et al. (2018), and we use the method proposed by Feng and Michaelides (2004). This method uses a fixed Cartesian mesh for fluid flow (the LBM lattice) and two sets of Lagrangian points. These Lagrangian points consist of N_l marker points $\mathbf{r}_{p,j}$ that follow the fluid and N_l reference points $\mathbf{r}^0_{p,j}$ that move by the rigid motion of the particles. In order to distribute the Lagrangian (marker and reference) points uniformly on the surface of each rigid sphere, we use the algorithm of Vogel (1979). During the simulation, the marker points are advected by the fluid, and any displacement between a marker point and its corresponding reference point leads to a Lagrangian force $\mathbf{\Lambda}_{p,j}(t)$. An explicit forcing scheme is implemented to compute this Lagrangian force using the

linear spring relationship

$$\mathbf{\Lambda}_{p,j}(t) = -\kappa \frac{a}{\Delta x^2}[\mathbf{r}_{p,j}(t) - \mathbf{r}^0_{p,j}(t)] \tag{7}$$

where the subscripts p and j count over the number of particles and Lagrangian points respectively. The force is weighted by the average surface area per Lagrangian point, $a = 4\pi R^2/N_l$. κ is the spring constant. The Lagrangian force is spread to the Eulerian fluid nodes according to

$$\mathbf{F}(\mathbf{x}, t) = \sum_{p,j} \mathbf{\Lambda}_{p,j}(t) D(\mathbf{q}_{p,j}), \tag{8}$$

which is then used as the body force (that is present only along the surface of each particle) in the LBM solver for the Navier-Stokes equations in the entire flow domain. Here, $\mathbf{q}_{p,j} = \mathbf{r}_{p,j}(t) - \mathbf{x}$ is the distance between the marker point and the Eulerian fluid node, and $D(\mathbf{q}) = \delta(q_x)\delta(q_y)\delta(q_z)/\Delta x^3$ is a Dirac delta distribution function where $\delta(x)$ is given by (Krüger et al., 2017)

$$\delta(x) = \begin{cases} 1 - |x|, & 0 \le |x| \le \Delta x \\ 0, & \Delta x \le |x| \end{cases} \tag{9}$$

The velocity $\mathbf{v}_{p,j}(t)$ of each marker point on each particle is computed from the fluid velocity by interpolation as

$$\mathbf{v}_{p,j}(t) = \sum_{\mathbf{x}} \mathbf{u}(\mathbf{x}, t) D(\mathbf{q}_{p,j}). \tag{10}$$

After interpolating the fluid velocity at the marker points, we update the marker positions by explicit Euler integration of

$$\frac{d\mathbf{r}_{p,j}}{dt} = \mathbf{v}_{p,j}. \tag{11}$$

To determine the required number of Lagrangian points on each particle, a test simulation of shear around a stationary sphere was performed. For a fixed particle radius (R = 4 lu), several values of N_l ranging from 300 to 1500 were used in these simulations to check the velocity profile through the centre of the sphere. In each of these simulations, the spring constant κ was varied between 0.002 and 2, and we chose κ = 0.002 because numerical instability was observed in suspension simulations with higher spring constants. No substantial difference was seen in the velocity profile inside the sphere for the number of Lagrangian points in this range and hence, we chose N_l = 800 (a = 0.25 lu^2) for all simulations. As another test of the accuracy of the chosen IBM, we computed the drag force on a sphere (with R = 4 lu) moving at a constant speed u_p = 0.002 lu/ts. To avoid the effects of periodic boundaries, we chose a large domain of size $100R \times 50R \times 50R$ lu with ν = 1/6 lu^2/ts. By comparing the computed force on the sphere with the expected Stokes drag force, we determined that the effective (hydrodynamic) radius of the sphere (R_{hyd}) was 4.2 lu, which is larger than the input radius R = 4 lu. Several authors (Ladd, 1994; Rohde et al., 2002; Feng and Michaelides, 2009; Krüger et al., 2011) have observed a hydrodynamic radius larger than the input radius, finding values of $R_{hyd} - R$ between $0.2\Delta x$ and $0.5\Delta x$. To make it simple for the reader, we use $R = R_{hyd}$ in all parameters that we report about the simulations; in the simulations, however, collisions are calculated using the input radius R = 4 lu.

2.4. Particle motion

Due to the shearing motion of the top and bottom walls, the flow starts to develop and the particles translate, rotate, and collide. As a result of the interaction between

the particles and liquid, each particle experiences a force $\mathbf{F}_p$, which is written as

$$\mathbf{F}_p = \sum_j -\mathbf{\Lambda}_{p,j}. \tag{12}$$

The particles' translational velocities $\mathbf{u}_p$ and positions $\mathbf{x}_p$ are updated by applying leapfrog integration to Newton's equations of motion

$$M\frac{d\mathbf{u}_p}{dt} = \mathbf{F}_p \tag{13}$$

$$\frac{d\mathbf{x}_p}{dt} = \mathbf{u}_p \tag{14}$$

where M is the mass of each particle, and the initial particle positions are randomly selected (Bernal, 1964; Finney, 2013) for each ϕ_v that is considered. Similarly, the torque $\mathbf{T}_p$ acting on a particle is

$$\mathbf{T}_p = \sum_j \mathbf{d}_{p,j} \times -\mathbf{\Lambda}_{p,j}(t) \tag{15}$$

where $\mathbf{d}_{p,j}$ is a vector from the center of mass of the p^{th} particle and its j^{th} marker point. We again apply leapfrog integration to the rotational equation of motion for a sphere

$$I\frac{d\boldsymbol{\omega}_p}{dt} = \mathbf{T}_p \tag{16}$$

and compute the angular velocity $\boldsymbol{\omega}_p$ of each particle starting from the initial condition $\boldsymbol{\omega}_p(t = 0) = 0$. The moment of inertia $I = (2/5)MR^2$ is a constant for all the particles. The rotation of each particle in the lattice reference frame is tracked by

computing the small angle rotation given by the matrix

$$\mathbf{R}_p(t) = \begin{pmatrix} 1 & -\omega_p^z \Delta t & \omega_p^y \Delta t \\ \omega_p^z \Delta t & 1 & -\omega_p^x \Delta t \\ -\omega_p^y \Delta t & \omega_p^x \Delta t & 1 \end{pmatrix} \tag{17}$$

where $\boldsymbol{\omega}_p = (\omega_p^x, \omega_p^y, \omega_p^z)$. The Lagrangian reference points are updated based on the new orientation of the particle at the end of a time step according to:

$$\mathbf{r}_{p,j}^0(t + \Delta t) = \mathbf{x}_p(t + \Delta t) + \mathbf{R}_p(t)[\mathbf{r}_{p,j}^0(t) - \mathbf{x}_p(t)] \tag{18}$$

2.5. Particle collisions

While simulating suspensions, collisions between particles are unavoidable, and hence a repulsive force is necessary to prevent overlap. As two particles collide, the size of the gap between the particles approaches the resolution of the simulation grid. After this time, the simulation can no longer resolve the flow of fluid between the particles accurately. Hence, we included an additional short range repulsive force when the gap width between the particles becomes less than a threshold ζ. The collision forces on a particle p due to another particle q and a wall w (top or bottom) are calculated as (Glowinski et al., 2001)

$$\mathbf{F}_{p,q}^{col} = \begin{cases} 0, & h > 2R + \zeta \\ \kappa_p \left(\dfrac{h - 2R - \zeta}{\zeta} \right)^2 \hat{\boldsymbol{n}}_{qp}, & h \le 2R + \zeta \end{cases} \tag{19}$$

$$\mathbf{F}_{p,w}^{col} = \begin{cases} 0, & s > R + \zeta/2 \\ \kappa_w \left(\dfrac{s - R - \zeta/2}{\zeta} \right)^2 \hat{\boldsymbol{n}}_{wp}, & s \le R + \zeta/2 \end{cases} \tag{20}$$

where $h = |\mathbf{x}_p - \mathbf{x}_q|$ is the distance between the particles and $s = |\mathbf{x}_p - \mathbf{x}_w|$ is the distance between the particle and the nearest point, $\mathbf{x}_w$, on the wall. $\hat{\boldsymbol{n}}_{qp}$ and $\hat{\boldsymbol{n}}_{wp}$ are unit vectors that connect the center of sphere p with sphere q and the wall. κ_p and κ_w specify the strengths of the repulsive forces. The collision forces are added to the IB force to obtain

$$\mathbf{F}_p = \sum_j -\mathbf{\Lambda}_{p,j}(t) + \sum_{q \neq p} \mathbf{F}^{col}_{p,q} + \sum_w \mathbf{F}^{col}_{p,w}. \tag{21}$$

The collision forces are always normal to the surface of the particles and therefore do not affect the torque.

In order to determine a suitable value of the repulsive force strength (κ_p) to suppress overlap, we performed simulations of two colliding rigid spheres with $R = 4$ lu each. The aspect ratios $\beta = L/H$ and $\Gamma = L/W$ (with $L = 100$ lu, $W = 50$ lu, and $H = 50$ lu) and the confinement ratio $\delta = 2R/H$ were 2, 2, and 0.17 respectively. The other parameters were $\nu = 1/30$ lu^2/ts and $Re_p = 0.33$. The initial gap width $(h - 2R)$ between the particles was $\approx 3R$, and the initial vertical (z) distance was $\approx 1.25R$. The threshold distance was $\zeta = 1$ lu.

When the flow starts to develop, the particles translate, rotate, and move closer. Fig. 2 shows a comparison between the gap widths of two colliding particles under several repulsive strengths κ_p. Starting from $\kappa_p = 0$, i.e. in the absence of collision force, we performed simulations with increasing κ_p up to 10. It is evident that the minimum gap width increases to the threshold distance, with a small difference between using $\kappa_p = 1$ or $\kappa_p = 10$. Although this simulation with two particles was stable with $\kappa_p = 10$, simulations of suspensions were unstable with this value. Instead, we chose $\kappa_p = 1$ for particle-particle collisions (which nonetheless maintains

gap widths close to the collision threshold) while retaining $\kappa_w = 10$ for particle-wall collisions for the simulations that follow.

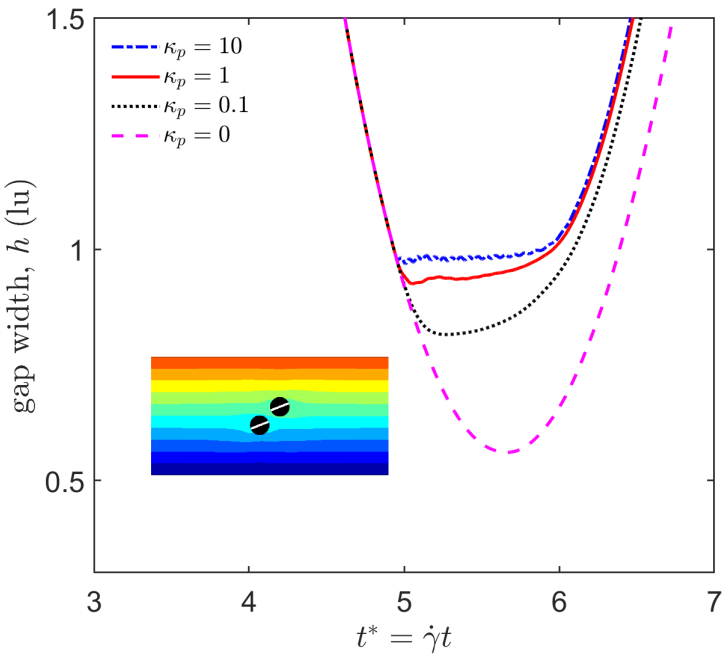

Figure 2: Gap width between two colliding particles as a function of time for several repulsive force strengths κ_p. Inset: sample visualisation of the cross-section through the colliding particles at an instant of time after the collision. The background is coloured according to the x component of the liquid velocity.

2.6. Implementation

The simulations were implemented using a custom C++ code. Simulations that involve a large domain size require significant memory, and the simulation time needed for the suspended particles to reach steady state conditions can take up to several days of computational time. Running the simulations on multiple processors and cores helps to keep the simulation times reasonable and makes larger domains and longer simulation times feasible. We therefore parallelised the custom immersed boundary lattice Boltzmann (IB-LB) code using the Message Passing Interface (MPI) library to implement full $3-D$ domain decomposition for the LBM fluid flow solver. This is achieved by dividing the simulation domain into several

subdomains and updating each subdomain independently while sharing data between them (Krüger et al., 2017). When simulating suspensions, the coupling of the particle motion with the fluid complicates the implementation of the $3-D$ domain decomposition because the Lagrangian points of a particle can be located in up to eight adjacent cuboid subdomains. Every MPI process stores a copy of the locations of all the particles and computes the contributions to the total force and torque on each particle that is (partially or completely) located within that subdomain. If a particle is located in more than one subdomain, then the total forces and torques on it are computed as a sum of the contributions from each subdomain. The results presented in the upcoming sections were obtained using two parallel processes on a 4 core Intel i7-6700 processor with 64 GB RAM. The suspension simulations required ≈ 0.5 GB of memory.

3. Validation studies

We discuss the validation of the implemented IB-LB method by performing two simulations: steady-state rotation of a single confined sphere and the trajectories of two interacting spheres, both in simple shear flow. The simulation of single particle rotation is compared with Bikard et al. (2006) and D'Avino et al. (2009), and the motion of two spheres is compared with Kulkarni and Morris (2008).

3.1. Simulation of freely rotating particle

The angular velocity ω_p of a sphere suspended in a sheared Newtonian liquid is (Einstein, 1906; Jeffery, 1922; Clift et al., 2005)

$$\omega_p = \frac{\dot{\gamma}}{2} \tag{22}$$

in the absence of inertia or wall effects. We computed the rotation rates of a sphere for varying particle-wall distances and a fixed particle radius. The confinement ratio δ was varied between 0.26 and 0.7 by using channel heights H between 32 and 12 lu. The aspect ratios were $\beta = 2$ & $\Gamma = 2$, and the liquid kinematic viscosity was 1/6 lu^2/ts. The shear speed U_w was varied to maintain a fixed particle Reynolds number. To ensure steady state, all the simulations ran for 20,000 time steps, and Fig. 3 presents the steady rotation rate of the sphere midway between two walls as a function of confinement ratio δ.

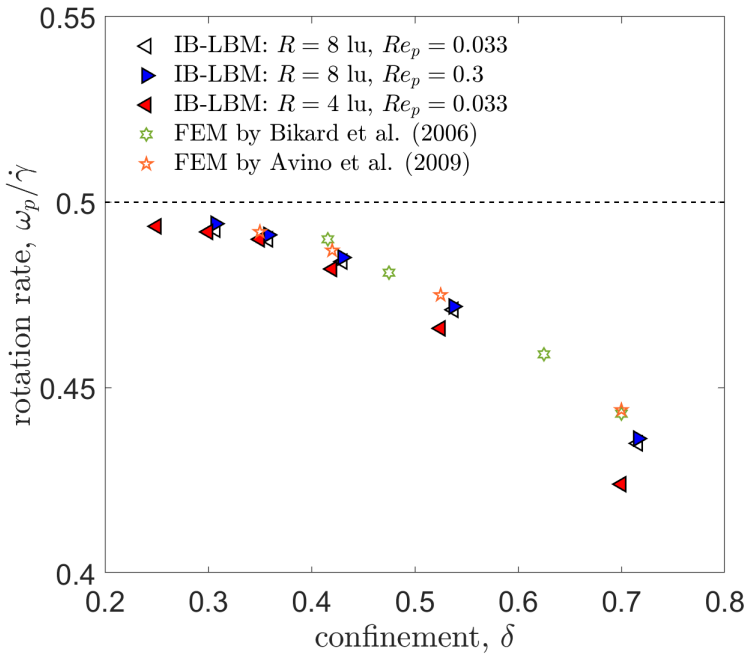

Figure 3: Steady rotation rate of a particle in shear between parallel plates as a function of the confinement δ at two different resolutions with $R = 4$ (filled red triangles) and 8 lu (open and filled blue triangles), and $Re_p = 0.033$ and 0.3. Dashed line shows the steady rotation rate in an unbounded domain.

The rotational speed of the particle decreases with increasing δ. For $\delta < 0.3$, the rotation rate approaches the theoretical value for unconfined shear (Eq. 22). Therefore wall effects become negligible for heights greater than $6R$, and confinement decreases the rotation rate noticeably for smaller heights. The computed rotation

rates agree with earlier computations (Bikard et al., 2006; D'Avino et al., 2009). For $\delta = 0.7$, however, the gap between the particle and wall is about 2 lu when $R = 4$ lu, and the discrepancy seen for high δ (filled red triangles in Fig. 3) is attributed to inadequate resolution of the flow in the gap between the particle and wall. At low confinements, the results approach the theoretical value.

Doubling the resolution of the simulations (domain dimensions and particle radius) while keeping all dimensionless parameters the same shows closer agreement with the other numerical results. To have the same average surface area per Lagrangian point ($a = 0.25$ lu^2) we quadrupled the number of Lagrangian points ($N_l = 3200$) and repeated the simulation of a freely translating sphere to compute the hydrodynamic radius. In this simulation, the domain was twice the size in the y (vorticity) and z (wall normal) directions, and 1.5 times in the x (shear) direction compared with the previous case (see Sec. 2.3). The effective radius R_{hyd} was computed to be 8.6 lu. In addition to increasing the resolution, we also considered the effect of increasing the particle Reynolds number by a factor 10 ($Re_p = 0.3$) on the rotation rate of the sphere (filled blue triangles in Fig. 3). It is evident that the effect of increasing the particle Reynolds number is not significant at least for these low values.

3.2. Trajectories of a pair of spheres

Approaching particles in a laminar shear flow may pass over each other, reverse their trajectories, or spiral, depending upon their initial conditions, as found by Kulkarni and Morris (2008) by means of (also) LB simulations. As a validation of our code, we performed a simulation where two particles of equal radii were initially separated by a vertical (z direction) distance of $\approx 2.5R$ and a horizontal

(x direction) distance of $\approx 10R$ and located at the same y position. The other simulation parameters were chosen to match the conditions of Kulkarni and Morris (2008) as follows: domain size $20R \times 20R \times 20R$, $U_w = 0.005$ lu/ts, $\nu = 1/30$ lu^2/ts, and therefore $Re_p = 0.1$. The simulation ran for 200,000 time steps, and Fig. 4 presents the trajectories of the two particles. The particles maintained a sufficient distance between them that inclusion of a collision model was not necessary.

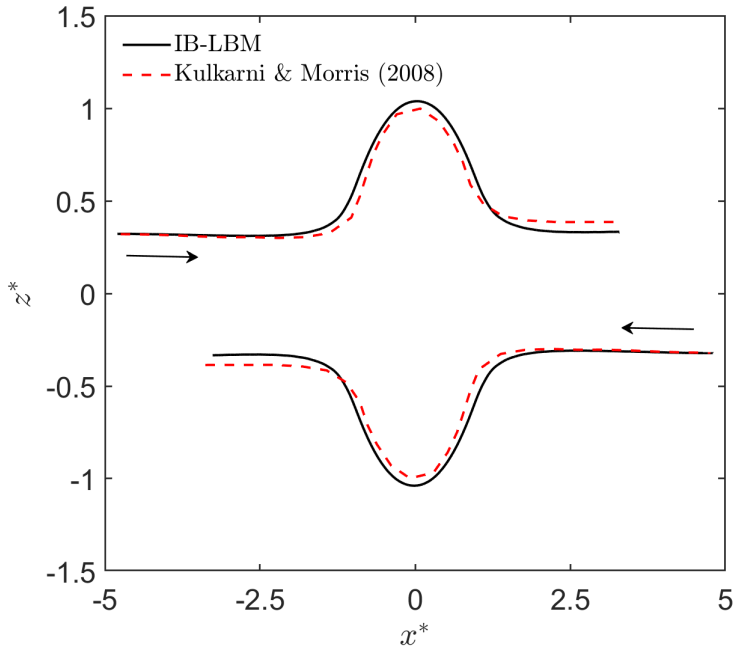

Figure 4: Trajectories of two particles in simple shear flow at $Re_p = 0.1$. Solid and dashed lines show the simulation results obtained by the present IB-LBM code and Kulkarni and Morris (2008), respectively. x^* and z^* are the particle positions scaled by particle radius and relative to the centre of the domain. Arrows indicate the direction of the motion.

When the shearing motion of the walls starts, the particles begin to translate and rotate. The particles approach each other from opposite directions, pass over each other, and then separate (indicated by the hump in Fig. 4). Comparing the trajectories of these particles with Kulkarni and Morris (2008), it is evident that the results are in good agreement even though the resolution is low ($R = 4$ lu).

4. Suspension simulations

We now turn our attention to simulations of monodisperse suspensions in simple shear flow. We report the response of the relative apparent viscosity of the suspension to the effects of shear rate, particle concentration, particle rotation, clustering, and changes in the shear rate (to a higher value and back to the initial value). In these simulations, we vary the particle Reynolds number between 0.11 and 0.55 by changing the shear speed. The aspect ratios β and Γ were 2 and 2, and confinement ratio $\delta = 0.17$ was kept constant in all the simulations that follow. The liquid kinematic viscosity $\nu = 1/30$ lu^2/ts. A solids volume fraction of 38% was used in all the simulations (except in Sec. 4.2), for which we simulate 310 particles with $R_{hyd} = 4.2$ lu.

4.1. Effects of shear rate

We investigated the rheological behaviour of the simulated suspensions for two different random initial particle configurations. Fig. 5 shows a sample $2-D$ visualisation of the $3-D$ simulated suspension at a moment in time. All particles have equal size and only those that intersect the mid-plane of the simulation domain are presented. For all shear rates, the same non-dimensional time range, $0 \leq \dot{\gamma}t \leq 400$, was computed. In order to evaluate the relative apparent viscosity of the suspension, we first computed the local shear stress τ as

$$\tau = \mu \frac{U_w - U_{xw}}{\Delta y} \tag{23}$$

where $\Delta y = 0.5$ lu is the distance between the wall and the adjacent fluid node, and U_{xw} is the x component of the liquid velocity in the two $x-y$ planes of nodes that

are adjacent to a wall. This local shear stress was evaluated at every lattice node in these two planes and then averaged to obtain the overall apparent viscosity (see Eq. 1).

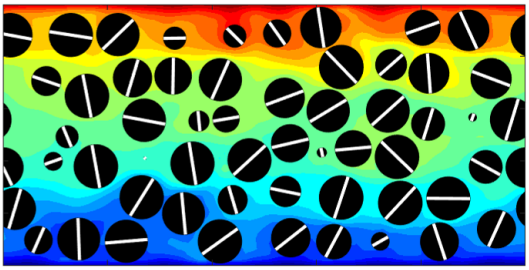

Figure 5: Visualisation of a cross-section through a simulated suspension in simple shear flow (ϕ_v = 38%, and Re_p = 0.55) at t^* = 17.6. The white lines in each circle show the orientation of the particle and the colours represent the x component of the interstitial liquid velocity scaled by the wall speed.

The evolution of the relative apparent viscosity over time in simulations at various shear rates (and therefore Re_p) is presented in Fig. 6. It is evident that the viscosity of the suspension fluctuates throughout the simulations due to the interactions of the particles with the interstitial liquid and walls, as well as the dynamic evolution of particle clusters. The effect of the shear rate can be seen from these figures. The viscosity of the suspension for Re_p = 0.11, 0.22, and 0.33 (top row of Fig. 6) decreases gradually and reaches a steady value. In contrast, at higher shear rates (Re_p = 0.44 and 0.55; bottom row of Fig. 6), the suspension viscosity increases at the beginning and then remains constant. In all these cases, the particles start from the same random initial positions. In the case of Re_p = 0.55 (bottom right of Fig. 6), for example, we can qualitatively say that the viscosity remains steady for $t^* > 200$. Hence, we evaluated a mean apparent viscosity (average of top and bottom) over this steady region of fluctuations and computed the standard deviation. The statistical steadiness of the fluctuations indicates that the rigid spheres

suspended in the liquid have reached a dynamic equilibrium. We followed the same averaging procedure for the simulations with the other particle Reynolds numbers and computed the average and standard deviation for each case (solid and dashed lines, respectively, in Fig. 6).

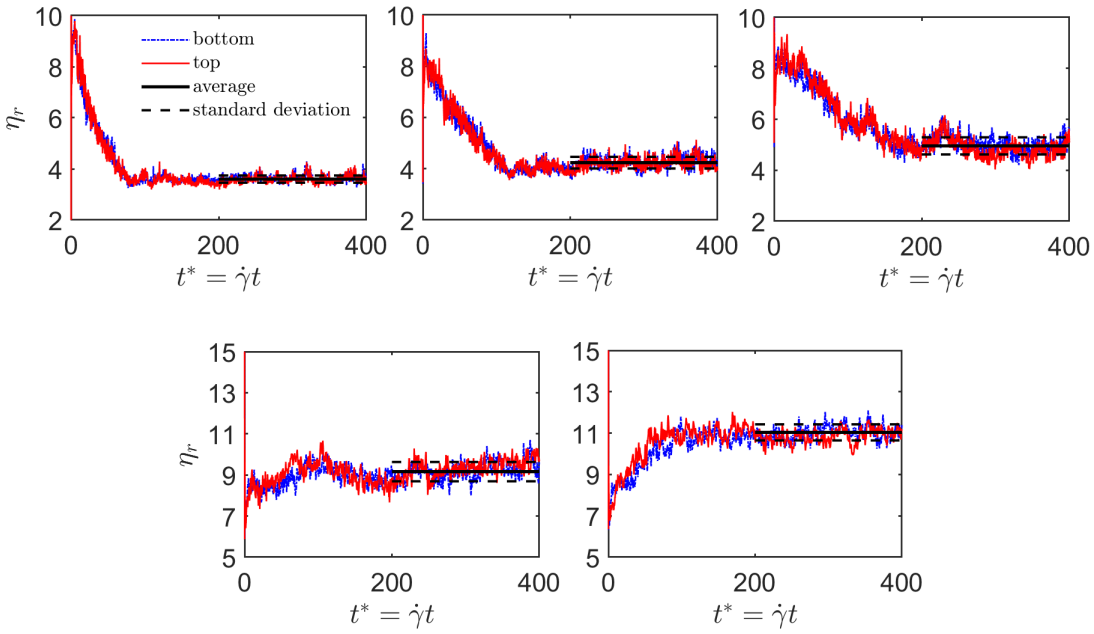

Figure 6: Relative apparent viscosity of a rigid sphere suspension as a function of time obtained for one random initial particle configuration (set 1) with $\phi_v = 38\%$. Top row: $Re_p = 0.11, 0.22, 0.33$. Bottom row: $Re_p = 0.44, 0.55$.

The relationship between the relative apparent viscosity and the shear rate (particle Reynolds number) for several random initial configurations is shown in Fig. 7. The apparent viscosity of the suspension increases with increasing particle Reynolds number, and the suspensions therefore exhibit shear thickening. This type of rheological behaviour was observed by Brady and Bossis (1985) for zero particle Reynolds number and areal packing fraction $\phi_A = 0.5$, by Picano et al. (2013) for $0.1 \leq Re_p \leq 10$ and $\phi_v = 0.30$, and by Javaran et al. (2014) for $0.1 \leq Re_p \leq 1$ and $\phi_v = 0.25$. In our

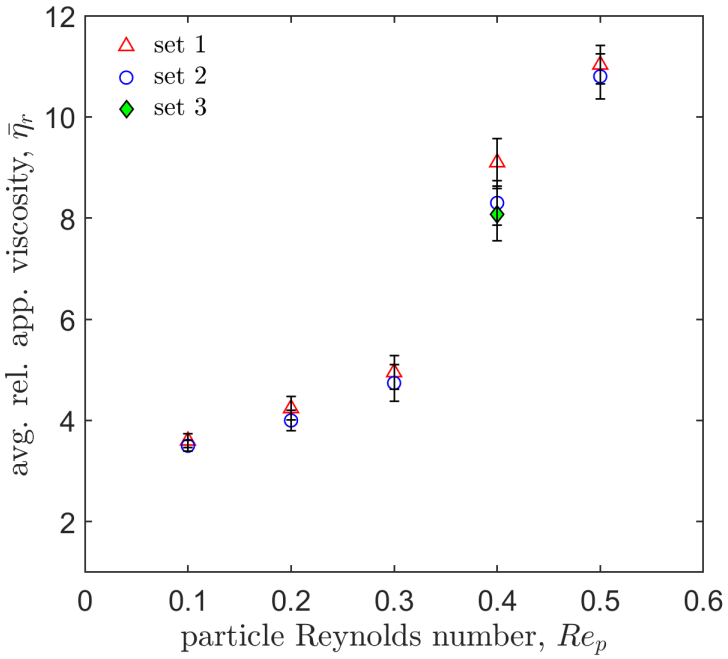

Figure 7: Average relative apparent viscosities (computed from top and bottom wall) of the suspensions at varying shear rates (and therefore Re_p) at a constant confinement ratio $\delta = 0.17$ for several random initial configurations of the particles. The third set (filled symbol) was computed only for $Re_p = 0.44$. For all cases, $\phi_v = 38\%$ and the errorbars show the standard deviations of the fluctuations.

simulations, we obtained similar values for the viscosities with two random initial particle configurations (set 1 and set 2), except at $Re_p = 0.44$. To understand the reason for the apparent discrepancy at $Re_p = 0.44$, we performed another simulation with a different initial configuration (set 3) and computed the average viscosity. The value for the third set agrees with the second.

Fig. 8 shows the fluctuations in the viscosity for the three sets of random initial particle positions at $Re_p = 0.44$. Since the fluctuations of the viscosities computed from the top and bottom walls follow similar trends (red and blue lines in Fig. 6), we show here the average of the values for the top and bottom walls. It is evident that the simulation viscosity of set 3 agrees closely with the results obtained for set 2. Though the viscosity for set 1 is typically higher than for the other two sets, all

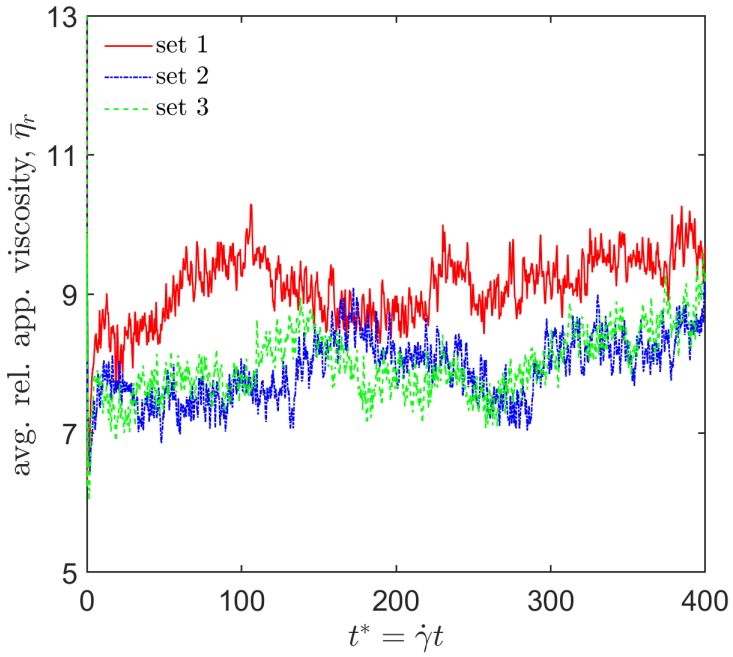

Figure 8: Fluctuations in the average relative apparent viscosities of the suspension for three random initial configurations at $Re_p = 0.44$ and $\phi_v = 38\%$.

three agree at $t^* \approx 150$. This suggests that the evolution of the relative apparent viscosity of the suspension may vary due to changes in the particle configuration. We verify this by cluster analysis in the following section.

4.2. Effects of particle concentration

To study the effects of particle concentration, we conducted a series of simulations for several particle Reynolds numbers $Re_p = 0.11, 0.33$, and 0.55. The solids volume fraction was varied from 2% to 38%, for which we simulated 20 to 310 spheres in a periodic box. The confinement ratio $\delta = 0.17$ and all the simulations ran for the same non-dimensional time duration ($\dot{\gamma}t = 400$). For validation of the IB-LBM code, we compared the average computed viscosities of the suspensions with several theoretical (Einstein, 1906; Batchelor and Green, 1972) and empirical expression (Vand, 1948; Krieger and Dougherty, 1959; Barnea and Mizrahi, 1973), as presented in Fig. 9.

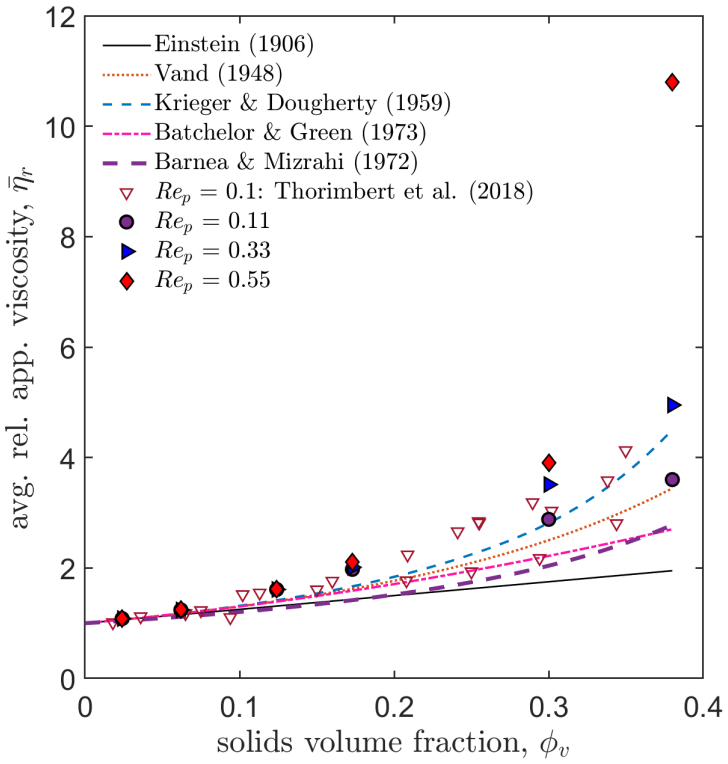

Figure 9: Average relative apparent viscosities of suspensions with varying solids volume fractions (computed based on R_{hyd}) as determined by theoretical and empirical expressions (solid and broken lines) and IB-LBM simulations (present work: filled symbols). The simulations of Thorimbert et al. (2018) at $Re_p = 0.1$ are also included (open triangles).

The apparent viscosity of the suspensions increases with increasing solids volume fraction. At a low particle Reynolds number ($Re_p = 0.11$), the simulation viscosities agree with Einstein (1906) for $\phi_v < 5\%$, Barnea and Mizrahi (1973) for $\phi_v < 10\%$, Batchelor and Green (1972) for $\phi_v < 15\%$, Krieger and Dougherty (1959) using the parameters $B = 2.5$ and a maximum packing fraction $\phi_v^{max} = 0.60$ (Bird et al., 2007) for ϕ_v up to 30%, as well as Vand (1948) for ϕ_v up to 38%. Recently, Thorimbert et al. (2018) reported values for apparent viscosities obtained through IB-LBM simulations (for $Re_p \leq 0.1$ and density ratio = 1.3). Our simulation viscosities are in good agreement with Thorimbert et al. (2018) at $Re_p = 0.1$ and ϕ_v up to 38%.

At higher solids volume fractions and higher particle Reynolds numbers, our

apparent suspension viscosities are higher than the empirical and theoretical correlations. Up to ϕ_v = 12%, Fig. 9 shows that the particle Reynolds number does not affect the apparent viscosity of the suspension. However, we start to observe the Reynolds number effect for simulations with $\phi_v \geq 17\%$ and $Re_p > 0.11$. We now present an analysis to demonstrate that these higher apparent viscosities are due to two phenomena, viz. the rotation of particles and clustering.

Fig. 10 presents histograms of the rotation rates of an arbitrary particle (left column) over the time of steady fluctuations ($200 \leq \dot{\gamma}t \leq 400$) and the rotation rates of all particles (right column) at $\dot{\gamma}t = 400$. Between the histograms, we show the fluctuation in the rotation rate of one particle over time. The solids volume fraction varies from 17% (top), 30% (middle) to 38% (bottom). The rotation rates are calculated for every particle within the region of steady fluctuations using a sampling interval of $\dot{\gamma}\Delta t = 20$. It is evident that, at low volume fraction (ϕ_v = 17%) and Re_p = 0.11 and 0.55, the particles on average rotate at a speed equal to the steady rotation rate in an unbounded domain (see Eq. 22). However, as the solids volume fraction increases, we start to observe the effect of Reynolds number on the rotational speed of the particles. At ϕ_v = 38% and Re_p = 0.55, we see that the particles rotate at a slower rate than for Re_p = 0.11. From these results we can see that both histograms show similar trends, and it is interesting that the particles temporarily rotate against the applied shear (indicated by negative $\omega_p/\dot{\gamma}$ in Fig. 10). Consistent with electrorheological fluids where an applied torque increases the rotation rate and decreases the apparent viscosity (Lemaire et al., 2008), we see that the apparent viscosity is higher when particles rotate slower. We also performed

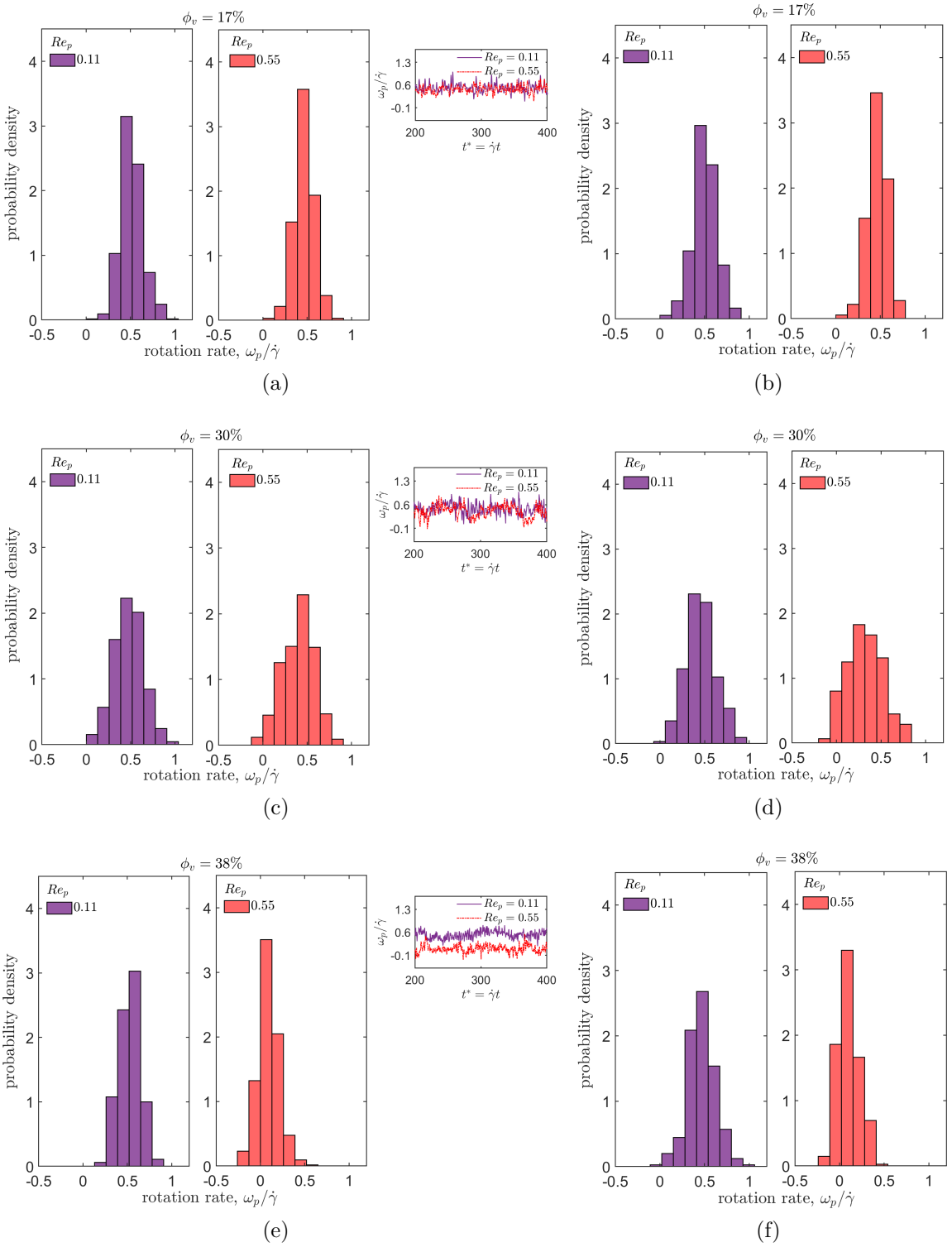

Figure 10: Left column (top to bottom): Distributions of the rotation rates of an arbitrary particle in a sheared suspension during $200 \leq \dot{\gamma}t \leq 400$. Right column (top to bottom): Histograms of the rotation rates of all the particles at a random time $\dot{\gamma}t = 400$. In both case $\phi_v = 17\%$, 30%, and 38%. Insets (in the middle) shows the rotation rate of a particle as a function of $\dot{\gamma}t$ during the steady fluctuations between 200 and 400.

simulations in which the angular velocity of all particles is fixed at zero. The details of these simulations, which exhibit a higher viscosity than the simulations with freely rotating particles, are provided in appendix A.

Another reason for an increased apparent viscosity at high Re_p and ϕ_v is the formation of particle clusters. It is intuitive that for a dilute suspension the particles are rather far away from each other and few clusters (groups of particles within a small distance h_c of each other, with $h_c \ll R_{hyd}$) will be present. With increasing solids fraction, more and larger clusters can be expected. We analysed the extent of clustering for the highest ϕ_v = 38% and Re_p = 0.55. In these simulations, we computed the number of clusters which are two or more particles. Appendix B details how the number of clusters depend on the threshold h_c (which we normalise by R_{hyd}). For small enough threshold, no clusters are found, whereas for a large enough threshold, all the particles would be counted as one cluster. In between, we find a maximum number of clusters for h_c/R_{hyd} = 0.083. Fig. 11 compares the evolution of apparent viscosity over time with the evolution of the number of clusters (for h_c/R_{hyd} = 0.083). With this threshold distance, we see that both the number of clusters and the apparent viscosity increase until $\dot{\gamma}t$ = 100 and then stabilise. Though we discuss only the case of ϕ_v = 38% and Re_p = 0.55, a brief discussion of the clustering behaviour in suspensions at low ϕ_v and Re_p is also given in appendix B.

All suspension simulations that have been presented so far were obtained in the same domain size given by $L \times W \times H$ (see Sec. 2.5). The sensitivity of our results to the size of the periodic domain (in the x and y directions) was examined by doubling the sizes in these directions. Other parameters such as ν, δ, and Re_p

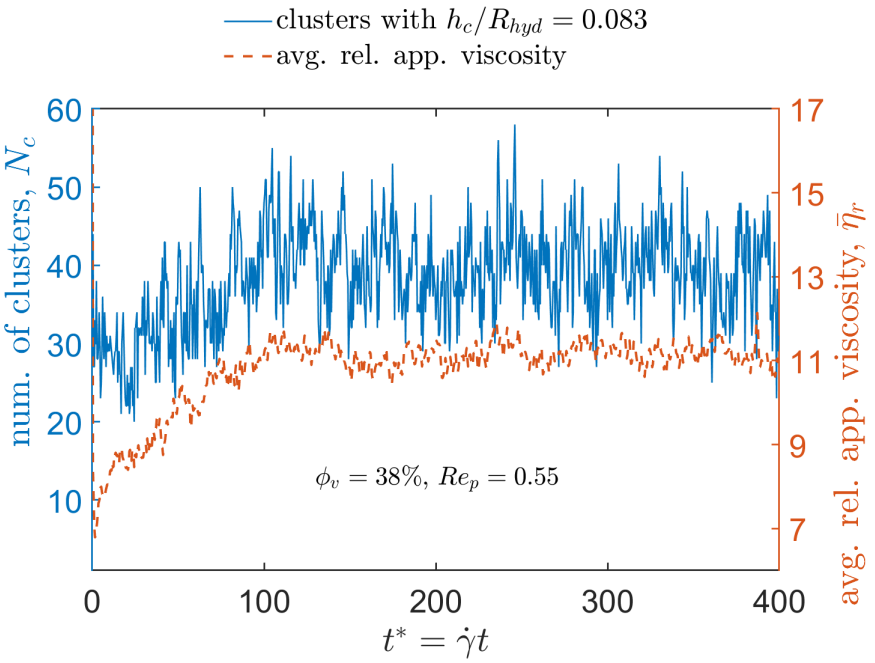

Figure 11: Evolution of the number of clusters and the relative apparent viscosity (average of top and bottom wall) as a function of time. The cluster threshold is $h_c/R_{hyd} = 0.083$, $Re_p = 0.55$, and $\phi_v = 38\%$.

were unchanged. Average relative apparent viscosities were computed and compared with the previous simulations. For $\phi_v = 31\%$ ($N_p = 1000$) and $Re_p = 0.55$, a 2% increase in the average viscosity value was observed. This could be because the solids volume fraction is increased by 1% compared with the earlier case where ϕ_v was 30% ($N_p = 240$). Hence, we consider that by doubling the simulation domain in the periodic directions, the results are not affected by a significant amount. However, the presence of physical walls in the wall normal (z) direction, introduces a confinement effect. An additional simulation with double the domain height (half the confinement ratio) was performed. For this simulation, we compared the average viscosity at $\phi_v = 31\%$ ($N_p = 500$) and $Re_p = 0.26$ with the previous simulation. We again observed a 2% increase in the average value of the apparent viscosity and therefore we conclude that the chosen value of $\delta = 0.17$ is sufficient to represent larger domains

with a small confinement effect.

Overall, we agree with Thorimbert et al. (2018) that replacing a spring-like repulsive force approach by a lubrication model is not necessarily required to arrive at satisfactory results for $Re_p \ll 1$. However, in addition to normal and tangential lubrication corrections, there may also be other sub-grid scale forces, for example colloidal forces, that may become important while studying the rheology of suspensions. Hence, inclusion of corrections that account for colloidal forcing are expected to produce more accurate rheological data for suspensions. The changes in the apparent viscosity of suspensions under various interparticle forces could be a topic of future investigation.

4.3. Simulations with changes in shear rate: History effects

Dense suspensions exhibit complex rheological characteristics, and the relative apparent viscosity of a suspension depends not only on the effects of shear rate and concentration, but may also depend on the duration of shearing and the previous shear history. Hence, we investigated the effects of step changes in the shear rate on the apparent viscosity of the suspensions. The parameters were identical to the previous simulations with ϕ_v = 38%. In this case, however, we changed the shear rate twice. We started the simulation with an initial shear rate $\dot{\gamma}_o = 6{\times}10^{-4}$ ts^{-1} (zone 1) up to $\dot{\gamma}_o t = 360$ and increased the shear rate to $\dot{\gamma}_f = 10^{-3}$ ts^{-1} (zone 2) and kept it constant for the same duration (up to $\dot{\gamma}_o t = 720$). Finally, we reduced the shear rate back to its initial value in the last part of the simulation (zone 3). The particle Reynolds numbers in the simulation changed between 0.33 and 0.55. Fig. 12 shows the variation in apparent viscosity as a function of time with sudden changes in the shear rate for three different random initial states.

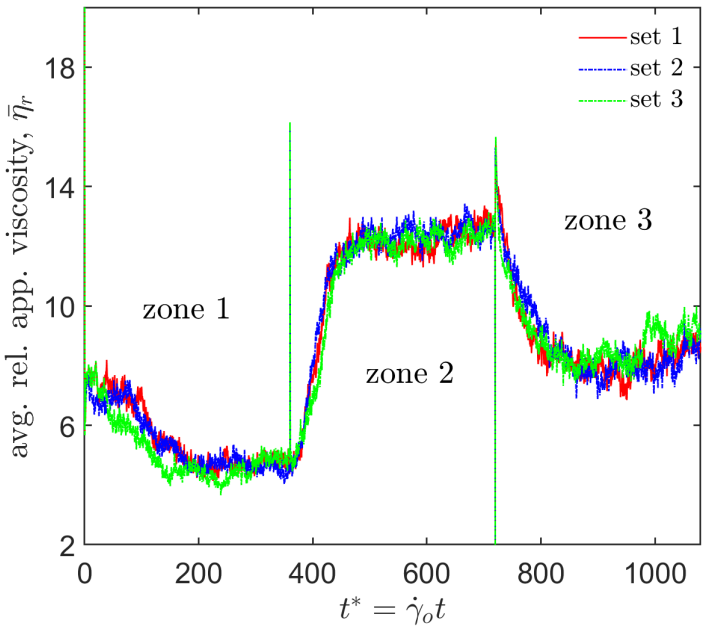

Figure 12: Fluctuations in the average relative apparent viscosity of the suspension as a function of time in a simulation with a varying shear rate computed for three random initial states. The particle Reynolds number changed between 0.33 in zone 1 and 0.55 in zone 2, to 0.33 back in zone 3 with $\phi_v = 38\%$

From the previous observations, we know that the shear stresses on the top and bottom walls follow similar trends, and hence in Fig. 12 we present only the average apparent viscosity. The peaks at $t^* = 360$ and 720 indicate the times of the changes in the shear rate. After the first change, the relative apparent viscosity of the suspension (for set 1, 2 & 3) retains its previous value (≈ 5) before it gradually increases to ≈ 12. This delay before the start of the increase is several times larger than the viscous timescale $\tau_\nu = (H/2)^2/\nu = 750$ ts ($\dot{\gamma}_o \tau_\nu = 0.45$). This indicates that the suspension temporarily remembers its previous shear history before it reaches a new configuration in zone 2. When the shear rate decreases back to its initial value, the suspended particles attain a different equilibrium viscosity (≈ 9) in zone 3 than at the end of zone 1. The end state of the suspended particles in each zone is the initial configuration for the next shear rate.

The reason for a different viscosity in zone 3 is that the spatial structure of the particle assembly differs from that of zone 1, which started with a random distribution. We used the same cluster cut-off (h_c/R_{hyd} = 0.083) as previously (see Fig. 11) to examine the transient evolution of particle clusters for the set 3 simulation presented in Fig. 12. From the number of clusters in each zone, it is noticeable from Fig. 14 (filled red triangles) that the particles form different cluster configurations in the three zones. For example, in the initial lower Reynolds number regime (zone 1, Re_p = 0.33) the suspension forms ≈ 4 clusters on average. After the first change in zone 2, the particle Reynolds number is higher than in zone 1 and the number of clusters increases. When the shear rate is brought back to its initial value, the particles attain a new cluster configuration different from that in zone 1. It is interesting to note that the trend in the evolution of the particle clusters follows the evolution of the relative apparent viscosity. From an average of ≈ 4 clusters in zone 1, the suspension gradually evolves over time to an average of ≈ 35 clusters in the high Reynolds number regime (zone 2) and decreases back to an average of ≈ 15 clusters in zone 3. These varying cluster configurations explains the differences in apparent viscosity. However, one might argue that the suspension viscosity in zone 3 could have reached the same value as at the end of zone 1 (≈ 5) if the suspension had been sheared for a longer time. If the viscosity in zone 3 were to eventually reach the same viscosity as in zone 1, the timescale of the change would be surprisingly long. From Fig. 12, we can estimate that the suspension takes a time $\Delta t \approx 100/\dot{\gamma}_o$ to reach a steady viscosity after the first change. For a particle with a 100 μm radius in water at Re_p = 0.3, this corresponds to a delay of 3.5 s.

In order to investigate whether increasing the shear time will bring the viscosity back to its initial value, we ran the set 3 simulation for a longer time. In this simulation, we increased the duration of each zone to $\dot{\gamma}_o \Delta t$ = 480. Average ap-

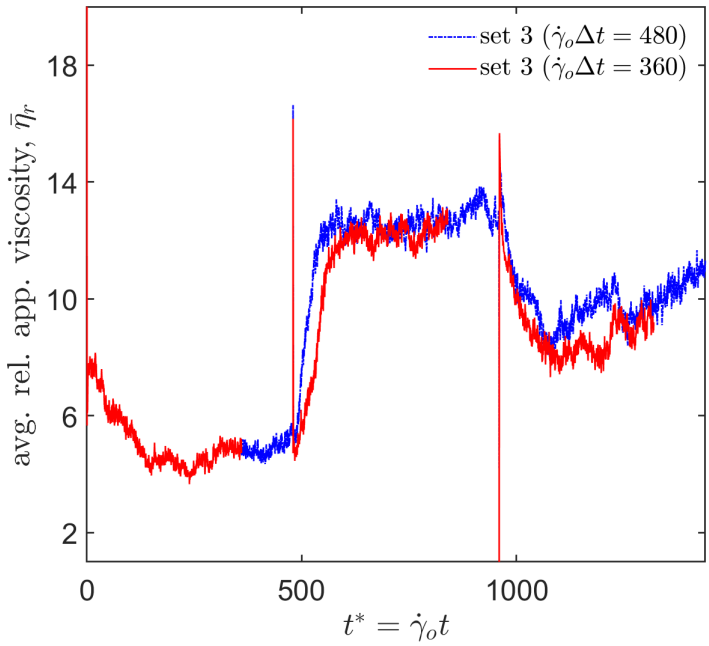

Figure 13: Effect of increasing the shear time on the relative apparent viscosity of the suspension for a random initial configuration (set 3) at ϕ_v = 38%. The particle Reynolds number in these simulations switches between 0.33 and 0.55 and the duration of shear in each zone is $\dot{\gamma}_o \Delta t$ = 480 and 360.

parent viscosity data for these longer simulation runs are shown in Fig. 13 along with the data from the earlier, shorter simulation. Though in the simulation with $\dot{\gamma}_o \Delta t$ = 360 the shear rate changes at $\dot{\gamma}_o \Delta t$ = 360 and 720, the data for this shorter simulation are plotted with gaps to match the times of the changes in shear rate of the longer simulation. We compare the two simulations that start with identical particle initial states, i.e. set 3, and see that the apparent viscosities obtained from these simulations do not match exactly in zones 2 and 3. This is because in each zone the structure of a particle assembly at the end of the longer simulation time (the broken blue lines in Fig. 13) is different from the structure at the end of the

shorter simulation time (the solid red line in Fig. 13). Considering the amplitude of fluctuations, however, the differences are not significant, and the result is effectively the same with the longer shear durations as with the shorter durations. From the cluster analysis of the longer run simulation (filled blue circles in Fig. 14), we infer that the suspension has a different structure in zone 3 than zone 1, which explains the difference in the apparent viscosity.

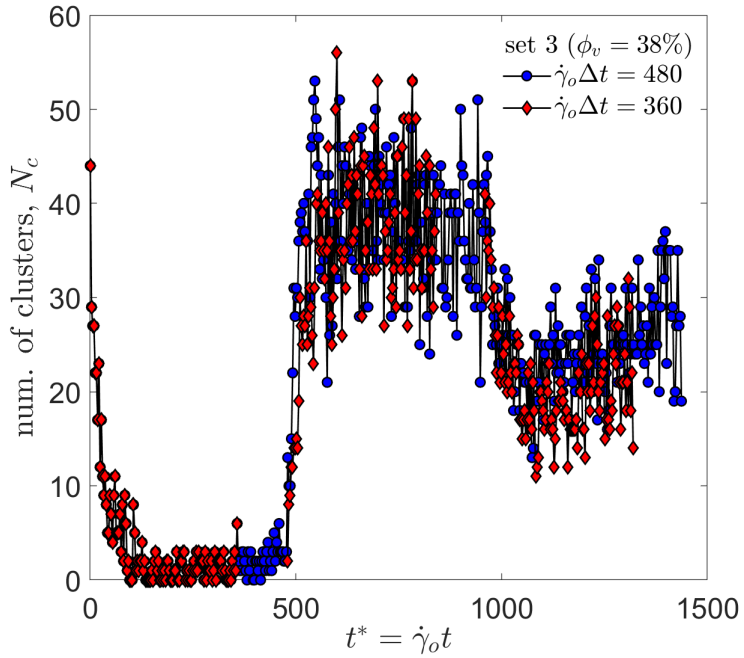

Figure 14: Evolution of particle clusters over time for a suspension with 38% solids. The particle Reynolds number switches between 0.33 in zone 1 to 0.55 in zone 2, and back to 0.33 in zone 3. The suspension is sheared for a time interval $\dot{\gamma}_o\Delta t$ = 360 in each zone of the shorter simulation and $\dot{\gamma}_o\Delta t$ = 480 in the longer simulation.

5. Conclusions

We implemented a three-dimensional, parallel, custom immersed boundary lattice Boltzmann method code and used it to simulate dense suspensions up to 38% solids by volume in simple shear flow. We used a repulsive spring force model to prevent overlap between particles during collisions. We validated the code by sim-

ulating two systems: the rotation of a single sphere under varying confinements δ and the trajectories of two spheres, both in simple shear flow. The simulations of one sphere at $Re_p = 0.03$ and 0.3 showed that for higher confinements the computed rotation rates are more accurate with a higher resolution, in agreement with earlier computations, and wall effects become negligible for $\delta \leq 0.3$. The simulation of a pair of spheres in simple shear at a particle Reynolds number of $Re_p = 0.1$ demonstrated the expected approach and separation of the particles.

Simulations of suspensions with varying shear rates $\dot{\gamma}$ showed shear thickening. Good agreement between the simulation viscosities and theoretical and empirical equations were observed for $Re_p = 0.11$ and solids volume fractions ϕ_v up to 38%. For $Re_p > 0.11$, the apparent viscosity of the suspension increased substantially with increasing Re_p. We found that this increase in the apparent viscosity is related to particle rotation and clustering. At higher particle Reynolds numbers and higher solids volume fractions, particles rotate slower, down to 35% of the imposed shear rate, than in more dilute suspensions (in which the average rotation rate is half the shear rate). Differences in cluster configuration and rotation speed contribute substantially to the momentum transport and underpin the variations in the suspension behaviour and so the apparent viscosity.

We investigated the effect of sudden changes in the shear rate on the apparent viscosity and cluster formation. We found that changes in shear rate lead to different cluster configurations and, hence, different apparent viscosities. Temporary shear at a higher rate lead to increased clustering, which was retained when the shear rate was returned to its initial value. The consequence was an increased apparent

viscosity due to the temporarily increased shear rate.

The simulations that were presented used a repulsive spring force model to handle particle collisions. We will next determine the effects of including a lubrication force correction (normal and tangential) on the apparent viscosity of the suspensions and modify the sub-grid scale force model to include surface potentials and colloidal forces. The effects of intermolecular forces on the clustering of particles are expected to influence both the steady apparent viscosity of the suspension and the re-configuration of suspensions in response to changes in the shear rate.

Acknowledgments

The authors acknowledge the financial support from the Synthesis and Solid State Pharmaceutical Centre (SSPC), funded by Science Foundation Ireland (SFI) and co-funded by the European Regional Development Fund under Grant Number 14/SP/2750. We greatly acknowledge the Irish Centre for High-End Computing (ICHEC) for the provision of computational facilities and support.

Appendix A

In this appendix, we discuss the hypothetical case of a suspension in which the particle do not rotate. For this purpose, we conducted two simulations (ϕ_v = 30% and 38%) at Re_p = 0.55 in which particle rotation was fully turned off by removing the update of the angular positions and angular velocities of the particles. This is equivalent to applying a time varying torque to every particle that exactly cancels the torque from the fluid. The result is that the angular velocity of all particles remains as zero. As shown in Table 1, the apparent viscosity is higher when the particle rotation is switched off than in the simulations where particles are allowed

to rotate freely (zero applied torque). We also conducted a cluster analysis (with h_c/R_{hyd} = 0.083) for ϕ_v = 38% and Re_p = 0.55 without particle rotations. In the range of steady fluctuations ($200 \leq \dot{\gamma}t \leq 400$), 35 clusters were observed on average for cases with and without particle rotations. This suggests that particle rotation affects the apparent viscosity but not the extent of clustering.

Table 1: Average apparent viscosities of suspensions computed in simulations with free particle rotation and no particle rotation at ϕ_v = 30% and 38%, and Re_p = 0.55.

ϕ_v	$\bar{\eta}_r$ (translation and free rotation)	$\bar{\eta}_r$ (only translation)
30%	3.9	5.3
38%	10.8	14.9

Appendix B

This appendix briefly discusses the effects of the particle Reynolds number on the average cluster size, $\bar{N}_p^c$ which is computed as

$$\bar{N}_p^c = \frac{N_p N_s}{N_c^t} \tag{24}$$

where N_p is the number of particles in the simulation, for instance, N_p = 310 for ϕ_v = 38%. N_c^t is the total number of clusters observed over N_s evenly spaced time intervals (including all single particles). The dependence of $\bar{N}_p^c$ on the choice of cut-off h_c is presented in Fig. 15 for two Reynolds numbers and three solids volume fractions. In all cases, the value of $\bar{N}_p^c$ starts at 1 and then increase to equal the number of particles N_p for large h_c. It can be seen that for ϕ_v = 38% and Re_p = 0.11 and 0.55, the increase in the average cluster size is steeper than in more dilute suspensions, and then stabilises for $h_c/R_{hyd} > 0.5$. The cluster threshold that was chosen to analyse the structure of the suspensions (0.083) coincides with the start of the increase in the average cluster size for ϕ_v = 38%. With this choice, clear changes

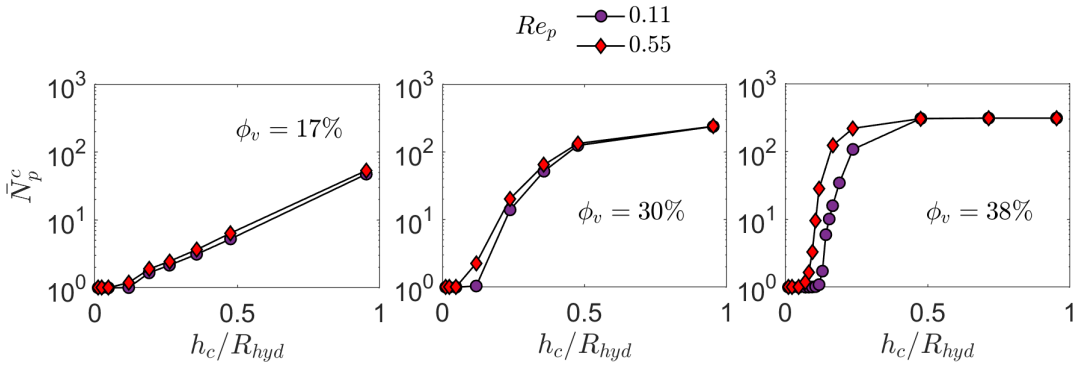

Figure 15: Average cluster size as a function of cluster threshold h_c/R_{hyd} for several solids volume fractions ϕ_v = 17%, 30%, and 38% at Re_p = 0.11 and 0.55.

in suspension structure are evident as a function of the solids volume fraction and particle Reynolds number. In Fig. 16 we present the evolution of the number of particle clusters (excluding single particles) as a function of time for several cut-off distances h_c/R_{hyd} ranging from 0.02 to 0.1 for ϕ_v = 38% and Re_p = 0.55. For h_c/R_{hyd} = 0.023, we hardly see any clusters and as the cut-off increases the number of clusters increases. For h_c/R_{hyd} = 0.083, we observed a maximum of 40 clusters on average, and the number of clusters decreases with further increase in h_c/R_{hyd}.

References

C K Aidun, Y Lu, and E J Ding. Direct analysis of particulate suspensions with inertia using the discrete Boltzmann equation. *Journal of Fluid Mechanics*, 373: 287–311, 1998.

E Barnea and J Mizrahi. A generalized approach to the fluid dynamics of particulate systems: Part 1. General correlation for fluidization and sedimentation in solid multiparticle systems. *The Chemical Engineering Journal*, 5(2):171–189, 1973.

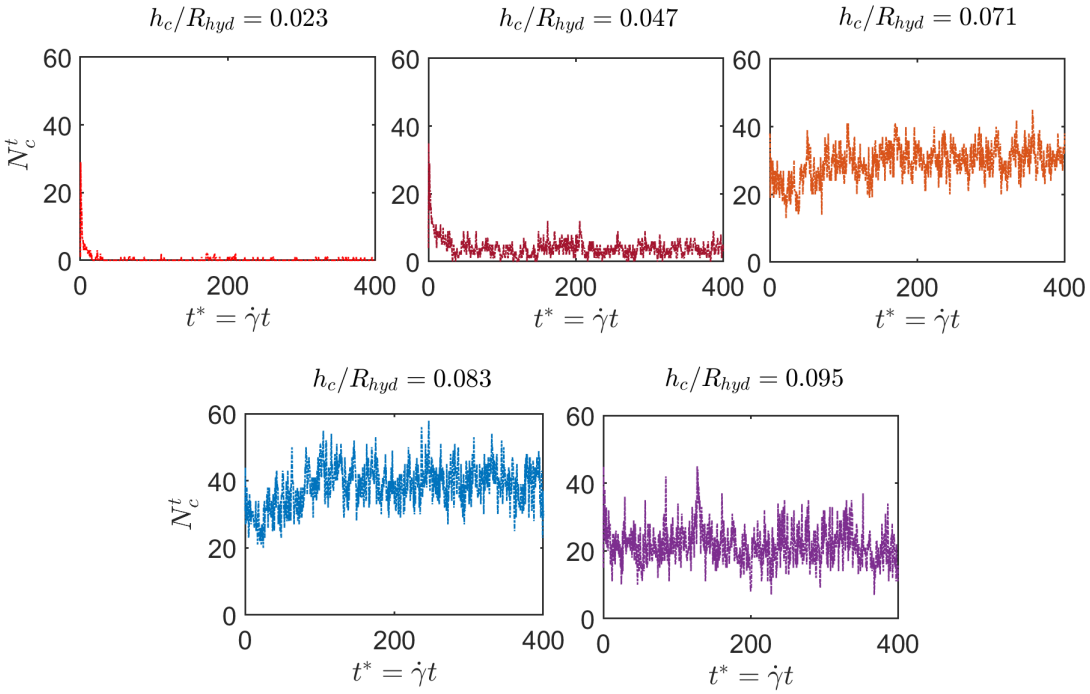

Figure 16: Transient evolution of particle clusters as a function of time for several cluster cut-off distances h_c/R_{hyd} ranging between 0.02 and 0.1. ϕ_v = 38% and Re_p = 0.55.

H A Barnes, J F Hutton, and K Walters. *An introduction to rheology*. Elsevier, 1989.

G K Batchelor and J T Green. The hydrodynamic interaction of two small freely-moving spheres in a linear flow field. *Journal of Fluid Mechanics*, 56(2):375–400, 1972.

J D Bernal. The Bakerian lecture, 1962. The structure of liquids. *Proceedings of the Royal Society of London. Series A, Mathematical and Physical Sciences*, 280 (1382):299–322, 1964.

P L Bhatnagar, E P Gross, and M Krook. A model for collision processes in gases. I. Small amplitude processes in charged and neutral one-component systems. *Physical Review*, 94(3):511, 1954.

J Bikard, P Menard, P D Edith, and T Budtova. 3D numerical simulation of the behaviour of a spherical particle suspended in a Newtonian fluid and submitted to a simple shear. *Computational Materials Science*, 37(4):517–525, 2006.

R B Bird, W E Stewart, and E N Lightfoot. *Transport phenomena*. John Wiley & Sons, 2007.

J F Brady and G Bossis. The rheology of concentrated suspensions of spheres in simple shear flow by numerical simulation. *Journal of Fluid Mechanics*, 155:105–129, 1985.

S Chen and G D Doolen. Lattice Boltzmann method for fluid flows. *Annual Review of Fluid Mechanics*, 30(1):329–364, 1998.

R Clift, J R Grace, and M E Weber. *Bubbles, Drops, and Particles (Dover Civil and Mechanical Engineering)*. Dover Publications, 2005.

G D'Avino, G Cicale, M A Hulsen, F Greco, and P L Maffettone. Effects of confinement on the motion of a single sphere in a sheared viscoelastic liquid. *Journal of non-Newtonian Fluid Mechanics*, 157(1-2):101–107, 2009.

J J Derksen. Numerical simulation of solids suspension in a stirred tank. *AIChE Journal*, 49(11):2700–2714, 2003.

J J Derksen. Eulerian-Lagrangian simulations of settling and agitated dense solid-liquid suspensions–achieving grid convergence. *AIChE Journal*, 64(3):1147–1158, 2018.

J J Derksen and H E A Van den Akker. Large eddy simulations on the flow driven by a rushton turbine. *AIChE Journal*, 45(2):209–221, 1999.

J J Derksen, G Reynolds, A Crampton, Z Huang, and J Booth. Simulations of dissolution of spherical particles in laminar shear flow. *Chemical Engineering Research and Design*, 93:66–78, 2015.

A Einstein. A new determination of molecular dimensions. *Ann. Phys.*, 19:289–306, 1906.

Z G Feng and E E Michaelides. The immersed boundary-lattice Boltzmann method for solving fluid–particles interaction problems. *Journal of Computational Physics*, 195(2):602–628, 2004.

Z G Feng and E E Michaelides. Robust treatment of no-slip boundary condition and velocity updating for the lattice-Boltzmann simulation of particulate flows. *Computers & Fluids*, 38(2):370–381, 2009.

J L Finney. Bernal's road to random packing and the structure of liquids. *Philosophical Magazine*, 93(31-33):3940–3969, 2013.

N A Frankel and A Acrivos. On the viscosity of a concentrated suspension of solid spheres. *Chemical Engineering Science*, 22(6):847–853, 1967.

M F Gadala and A Acrivos. Shear-induced structure in a concentrated suspension of solid spheres. *Journal of Rheology*, 24(6):799–814, 1980.

R Glowinski, T W Pan, T I Hesla, D D Joseph, and J Periaux. A fictitious domain approach to the direct numerical simulation of incompressible viscous flow past

moving rigid bodies: Application to particulate flow. *Journal of Computational Physics*, 169(2):363–426, 2001.

E Guazzelli and O Pouliquen. Rheology of dense granular suspensions. *Journal of Fluid Mechanics*, 852, 2018.

E J Javaran, M Rahnama, and S Jafari. Particulate flow simulation using lattice Boltzmann method: A rheological study. *Advanced Powder Technology*, 25(4): 1325–1333, 2014.

G B Jeffery. The motion of ellipsoidal particles immersed in a viscous fluid. *Proceedings of the Royal Society of London. Series A*, 102(715):161–179, 1922.

I M Krieger and T J Dougherty. A mechanism for non-Newtonian flow in suspensions of rigid spheres. *Transactions of the Society of Rheology*, 3(1):137–152, 1959.

T Krüger, F Varnik, and D Raabe. Efficient and accurate simulations of deformable particles immersed in a fluid using a combined immersed boundary lattice Boltzmann finite element method. *Computers & Mathematics with Applications*, 61 (12):3485–3505, 2011.

T Krüger, H Kusumaatmaja, A Kuzmin, O Shardt, G Silva, and E M Viggen. *The lattice Boltzmann method: Principles and practice*. Springer, 2017.

P M Kulkarni and J F Morris. Pair-sphere trajectories in finite-Reynolds-number shear flow. *Journal of Fluid Mechanics*, 596:413–435, 2008.

A J C Ladd. Numerical simulations of particulate suspensions via a discretized

Boltzmann equation. Part 1. Theoretical foundation. *Journal of Fluid Mechanics*, 271:285–309, 1994.

E Lemaire, L Lobry, N Pannacci, and F Peters. Viscosity of an electro-rheological suspension with internal rotations. *Journal of Rheology*, 52(3):769–783, 2008.

S Mueller, E W Llewellin, and H M Mader. The rheology of suspensions of solid particles. *Proceedings of the Royal Society A: Mathematical, Physical and Engineering Sciences*, 466(2116):1201–1228, 2009.

J M Peterson and M Fixman. Viscosity of polymer solutions. *The Journal of Chemical Physics*, 39(10):2516–2523, 1963.

F Picano, W-P Breugem, D Mitra, and L Brandt. Shear thickening in non-brownian suspensions: An excluded volume effect. *Physical Review Letters*, 111(9):098302, 2013.

K Rietema. Science and technology of dispersed two-phase systems - I and II. *Chemical Engineering Science*, 37(8):1125–1150, 1982.

M Rohde, J J Derksen, and H E A Van den Akker. Volumetric method for calculating the flow around moving objects in lattice-Boltzmann schemes. *Physical Review E*, 65(5):056701, 2002.

X Shan and H Chen. Lattice Boltzmann model for simulating flows with multiple phases and components. *Physical Review E*, 47(3):1815, 1993.

O Shardt and J J Derksen. Direct simulations of dense suspensions of non-spherical particles. *International Journal of Multiphase Flow*, 47:25 – 36, 2012.

A Ten Cate, J J Derksen, L M Portela, and H E A Van den Akker. Fully resolved simulations of colliding monodisperse spheres in forced isotropic turbulence. *Journal of Fluid Mechanics*, 519:233–271, 2004.

Y Thorimbert, F Marson, A Parmigiani, B Chopard, and J Lätt. Lattice Boltzmann simulation of dense rigid spherical particle suspensions using immersed boundary method. *Computers & Fluids*, 166:286–294, 2018.

S Tschisgale, T Kempe, and J Fröhlich. A general implicit direct forcing immersed boundary method for rigid particles. *Computers & Fluids*, 170:285–298, 2018.

V Vand. Viscosity of solutions and suspensions. I. Theory. *The Journal of Physical Chemistry*, 52(2):277–299, 1948.

H Vogel. A better way to construct the sunflower head. *Mathematical biosciences*, 44(3-4):179–189, 1979.

Y Yoshida, T Katsumoto, S Taniguchi, A Shimosaka, Y Shirakawa, and J Hidaka. Prediction of viscosity of slurry suspended fine particles using coupled DEM-DNS simulation. *Chemical Engineering*, 32, 2013.